

In the format provided by the authors and unedited.

# Intertwined superfluid and density wave order in two-dimensional $^4\text{He}$

Ján Nyéki<sup>1</sup>, Anastasia Phillis<sup>1</sup>, Andrew Ho<sup>1</sup>, Derek Lee<sup>2</sup>, Piers Coleman<sup>1,3</sup>,  
Jeevak Parpia<sup>4</sup>, Brian Cowan<sup>1</sup>, John Saunders<sup>1\*</sup>

<sup>1</sup>Department of Physics, Royal Holloway University of London, Egham, Surrey, TW20 0EX, U.K.

<sup>2</sup>Department of Physics, Blackett Laboratory, Imperial College London, London SW7 2AZ, U.K.

<sup>3</sup>Center for Materials Theory, Department of Physics and Astronomy, Rutgers University, Piscataway, NJ 08854, USA.

<sup>4</sup>Department of Physics, Cornell University, Ithaca, NY 14853, USA.

\*e-mail: j.saunders@rhul.ac.uk

## Contents

<b>1</b>	<b>Methods</b>	<b>2</b>
1.1	Torsional oscillator and thermometry . . . . .	2
1.2	Coverage scale . . . . .	3
1.3	Composite background . . . . .	4
<b>2</b>	<b>On the structure of the second layer</b>	<b>5</b>
2.1	From liquid gas coexistence region to uniform fluid . . . . .	7
2.2	Transition from uniform fluid to phase with broken translational symmetry . . . . .	8
2.3	Anomalous superfluid coverage regime . . . . .	8
<b>3</b>	<b>Calibration of superfluid density</b>	<b>11</b>
<b>4</b>	<b>Scaling the data</b>	<b>13</b>
<b>5</b>	<b>Superfluid density from excitation spectrum ansatz.</b>	<b>15</b>
<b>6</b>	<b>Trial wavefunction for intertwined superfluid and density wave order</b>	<b>17</b>
<b>7</b>	<b>Non Abelian Manifold</b>	<b>19</b>
<b>8</b>	<b>Quantum transition</b>	<b>21</b>

## 1 Methods

*In this section we provide details of the torsional oscillator, sample thermalization to low mK temperatures, and thermometry. We outline the measurement techniques and describe how the coverage scale is defined. We discuss the determination of the torsional oscillator composite background, which allows us to extract the signal arising from superfluid mass decoupling.*

### 1.1 Torsional oscillator and thermometry

The double torsional oscillator is shown in Fig. S1; it is machined (apart from the cell lid) from a single piece of coin silver. The hollow upper part is filled with 48 sheets of exfoliated graphite [33], 130  $\mu\text{m}$  thick, each diffusion bonded onto silver foils 25  $\mu\text{m}$  thick for thermalisation. Each silver foil is diffusion bonded to the base of the upper part of the cell ensuring good thermalisation down to the lowest temperatures of 1mK. The cell lid is glued in place using Stycast 2850 FT epoxy. The lower part of the double oscillator is a solid coin silver cylinder of diameter 20 mm. The two torsion rods are coin silver of outer diameter 2.5 mm and 2.0 mm respectively. They are hollow to permit the admission of helium to form the surface film on the graphite substrate, via a filling capillary from room temperature. Two magnesium electrodes are glued to this cylinder; in operation they are biased at 50V. The double oscillator is mounted on a massive copper isolation mass of estimated resonance frequency 80 Hz to reduce levels of vibrational noise at the oscillation frequencies. The double oscillator had resonant frequencies at low temperatures of 1423 Hz (anti-symmetric mode) and 277 Hz (symmetric mode). All measurements reported were taken with the antisymmetric mode, since the symmetric mode had insufficient frequency stability. The mass sensitivity is  $-9.33 \text{ mHz}/\text{cm}^3\text{STP}$  of  $^4\text{He}$ , Fig. S2. The frequency resolution  $\Delta f/f$  in the antisymmetric mode was  $2 \times 10^{-9}$ .

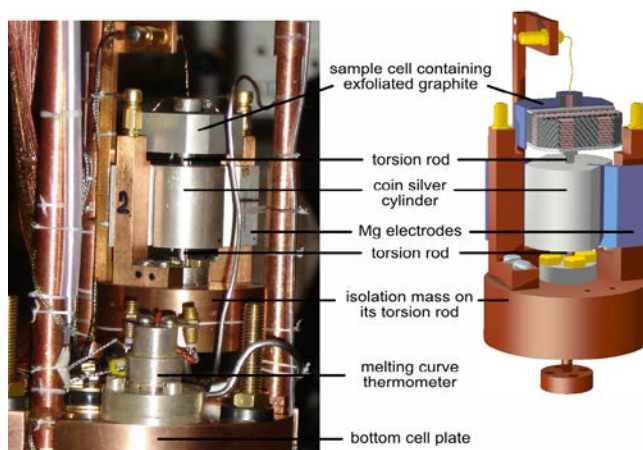


**Fig. S1.** Torsional oscillator used in our experiments. Cross-sectional view (right) shows assembly details of exfoliated graphite and silver foils.

This work necessitated measurements over a wide temperature range, from 1 mK to 3 K. Therefore the oscillator assembly and associated thermometry are mounted on a copper cell plate that is in turn mounted via brass support rods with insulating (vespel) washers to the top of a copper nuclear adiabatic demagnetisation stage. The cell plate is cooled through a weak thermal link, consisting of copper braid. Importantly this allows us to sweep temperature (the cell plate can be heated to 710 mK with power 350  $\mu\text{W}$  while maintaining circulation of the dilution refrigerator), at the expense of minimum temperature (1.2 mK). Thermometry to cover the entire temperature range with high precision is provided by a carbon glass thermometer (above 1.3 K), germanium thermometer (50 mK to 6 K) (calibration provided by manufacturer) and a  $^3\text{He}$  melting curve thermometer (1 mK to 250 mK), using the superfluid A transition as a fixed point.

The resonance frequency and quality factor of the torsional oscillator are measured as a function

of temperature. Most data is taken sweeping the temperature at a suitable rate to maintain thermal equilibrium, checked by points taken at stabilised temperature (using the appropriate thermometer and digital temperature control implemented using LabVIEW data acquisition software). The drive and detection electrodes are mounted on the copper isolator block, with a typical capacitance to the biased electrode of 11 pF. The oscillator is driven on (or close to) resonance, applying a typical drive voltage of 9.9 mV from an Agilent DS345 function generator using an HP5335A counter to provide a high stability reference clock (aging rate  $< 5 \times 10^{-10}$  per day). The current induced in the detection electrode is measured by a Brookdeal 5002 current preamplifier, with subsequent lockin-detection. We measure the real and imaginary parts of the response, to determine the resonant frequency and quality factor of the oscillator.

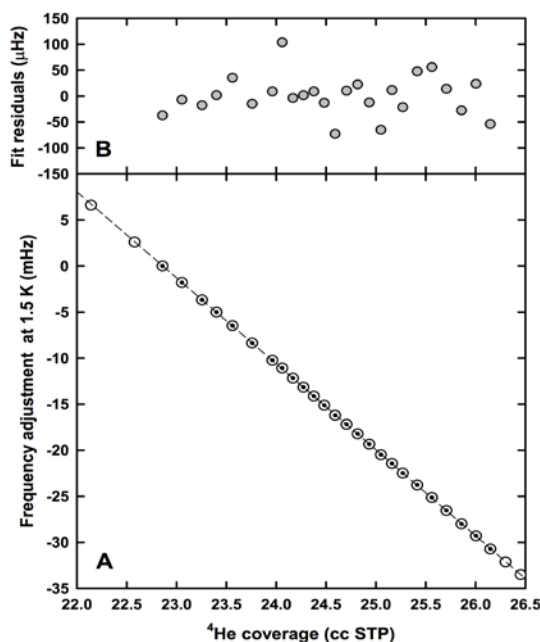


**Fig. S2.** Mass loading calibration at 1.5 K for coverages between  $17.11 \text{ nm}^{-2}$  and  $19.57 \text{ nm}^{-2}$  (filled circles). The upper panel shows residuals of a linear fit. These residuals also reflect the long term frequency stability of the oscillator.

We can determine the phase angle between drive and detect signals (with precision  $< 0.1^\circ$ ) by calibrating the response of the oscillator through a frequency sweep at a chosen reference temperature. This measurement provides a reference value for the quality factor  $Q$ ,  $Q_R$ , and the amplitude at resonance  $A_R$ . In subsequent measurements we drive the oscillator at fixed frequency  $f_D$  and drive voltage and measure the quadrature  $X$  and in-phase response  $Y$ . The resonance frequency is the drive frequency at which we obtain a null response of the in-phase signal. In practice we operate within  $5 \mu\text{Hz}$  of resonance, beyond which the drive frequency is re-tuned. Then:  $Q = \frac{X^2 + Y^2}{X} \left( \frac{Q_R}{A_R} \right)$  and  $f = f_D \left( 1 + \frac{Y}{X} \frac{1}{2Q} \right)$ . Typically the amplitude of oscillation at edge of cell is 6 nm. We note that this is more than an order of magnitude greater than the lattice parameter in the completed second layer.

## 1.2 Coverage scale

Helium is adsorbed onto the exfoliated graphite surface from a room temperature gas handling system. Doses of helium gas are added from a calibrated standard volume, at a precisely measured pressure. To convert from  $\text{STPcm}^3$  of gas to film density we perform a  $^4\text{He}$  vapour pressure isotherm at 4.2 K [34]. For our sample, point-B of a dead volume corrected vapour pressure isotherm corresponds to 15.23

$\text{cm}^3$ . We define our coverage scale by setting the coverage at this point, corresponding to second layer promotion, to  $11.40 \text{ nm}^{-2}$ . The change in oscillator frequency due to mass loading, measured at 1.5K, is shown in Fig. S2. This mass-loading shift is applied to all the frequency data discussed in this paper.

### 1.3 Composite background

In torsional oscillator experiments it is necessary to perform a background subtraction in order to infer the frequency shift and dissipation arising from potential superfluidity. However the temperature dependence of the frequency shift and dissipation observed with a non-superfluid sample differs from that of the empty oscillator. This is illustrated in Fig. S3, which shows two reference samples (at coverages  $17.11 \text{ nm}^{-2}$  and  $19.96 \text{ nm}^{-2}$ ), spanning the coverage range over which a superfluid response is detected. These clearly differ from the empty cell background, and this is attributed to the viscoelastic response of exfoliated graphite coated by a non-superfluid film. Also shown is a sample at coverage  $18.09 \text{ nm}^{-2}$ , which had the largest superfluid response.

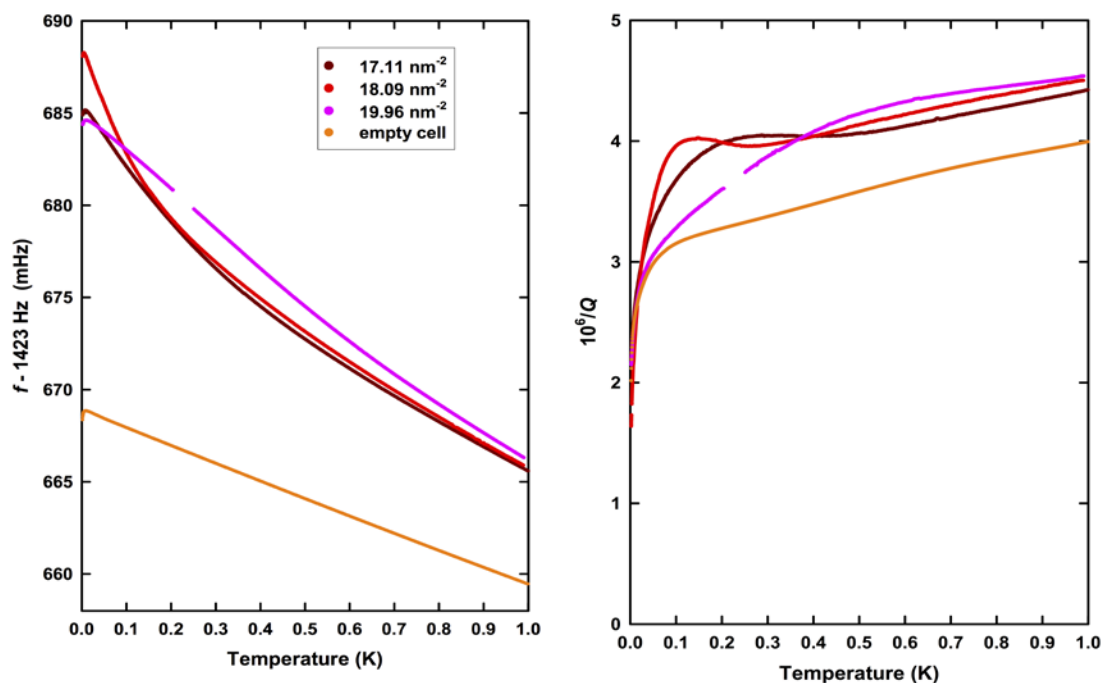


**Fig. S3.** Temperature dependence of the resonance frequency and dissipation of empty cell compared to that of cell loaded with different samples. Frequency data for different coverages are shifted by measured mass sensitivity (Fig. S2).

We construct a composite background, as is the norm in torsional oscillator studies of helium films [52]. In our case the composite background is generated as follows. We take the  $17.11 \text{ nm}^{-2}$  reference sample as an initial background. We then correct it, at each coverage, by a function to eliminate the high temperature frequency shift, which features a maximum around 0.5 K, which monotonically evolves with coverage. This correction  $\Delta f^{\text{corr}}(T)$  is determined from fits to each frequency shift data set using the form  $\Delta f^{\text{corr}}(T) = \Delta f_0 + kx^2 / \cosh^2 x$  where  $x = \Delta_h / (T + T_h)$ . These fits are performed over a temperature range well-separated from that in which superfluid response is observed. In the example shown in Fig. 1E, coverage  $19.02 \text{ nm}^{-2}$ , the temperature range of the fit is 0.1K to 0.95K. The dependence of the fit parameters on coverage is shown in Fig. S4. The parameters governing the temperature dependence,  $\Delta_h$  and  $T_h$  are essentially coverage independent. The parameter  $k$  governs the magnitude of the local maximum in frequency shift around 0.5K. The parameter  $\Delta f_0$  is a small

temperature independent offset. Close to third layer promotion, at  $20 \text{ nm}^{-2}$  it is larger than the frequency shift due to superfluidity, and is the chief source of the errors shown in Fig. 1F.

The dissipation does not have a simple temperature dependence, so it is not possible to generate a composite background in this case. Therefore, throughout the paper, dissipation data are presented with only the empty cell background subtracted. However, the systematics of the evolution of the dissipation with helium coverage, provides insight into the second layer phase diagram, as discussed in the following.

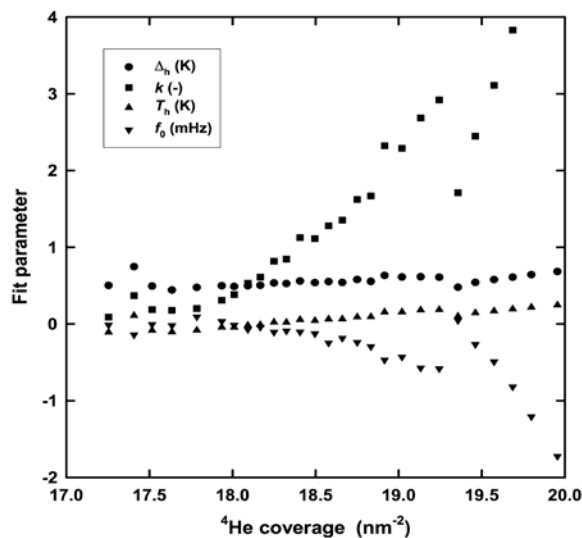


**Fig. S4.** Coverage dependence of parameters used in composite background

## 2 On the structure of the second layer

*We briefly describe the status of theoretical predictions of the evolution of the structure of the second layer of helium as a function of coverage. We elaborate on the systematics of the coverage dependence of the torsional oscillator response observed in our experiments, particularly dissipation. These provide evidence for a sequence of phase changes in the second layer as the coverage is increased, which correlate with the onset of superfluid response. No definitive identification of structure is possible from these measurements alone. Nevertheless the evidence for intertwined superfluid and density wave order derives from the nature of the superfluid response itself.*

There is theoretical consensus [35, 36, 37, 38] that the second layer of helium on graphite self-condenses at a density between  $4$  and  $5 \text{ nm}^{-2}$ , with a critical temperature of order  $0.8\text{K}$ . At coverages below this value, the second layer consists of self-bound two-dimensional liquid droplets. At coverages immediately above this value a uniform two dimensional fluid is expected.

Close to the coverage at which promotion to a third layer occurs the second layer is predicted to be an incommensurate (i.e not in registry with the first layer) 2D solid on a triangular lattice [37, 38]. At slightly lower coverages there is debate over whether the second layer initially forms a commensurate solid, registered with the first layer triangular lattice, out of the uniform fluid phase as its density is increased. This phase (the C-phase) can be thought of as structure in which both the first and second layer form a triangular superlattice with respect to a fictitious triangular grid. The ratio of the density of the second layer to the first layer of such possible superlattices is then a rational number eg  $7/13$ ,  $9/16$ ,  $4/7$ ,  $7/12$ ,  $12/19$ ,  $13/19$ . The superlattices considered to be relevant to the second layer prior to

third layer promotion are the 4/7 and 7/12 phases. It is at densities around these putative C-phases that the anomalous superfluid response we report is observed.

For  $^4\text{He}$  films, early Path Integral Monte Carlo (PIMC) simulations [37] found the 4/7 phase. However more recent calculations [38, 41] find that the 7/12 structure is more stable than the 4/7 structure. These latter authors also conclude that both structures are *unstable* with respect to a liquid phase, but differ concerning the reasons. [38] argues that zero-point motion of first layer  $^4\text{He}$  atoms is responsible while [41], which concerns graphene as a substrate, argues that quantum exchange of second layer atoms is the main effect. [38] uses a laterally averaged helium-graphite potential for simulations of the second layer. On the other hand [42] use an anisotropic helium-graphite potential reflecting the surface corrugation. This stabilizes a high density first layer commensurate structure and these authors find that a 4/7 structure in the second layer is at least metastable on top of this first layer commensurate structure. The potential importance of using the full helium-graphite potential is also highlighted by neutron scattering data [43, 44] which find evidence for commensurate structures in the first layer which develop around promotion to the third layer in both  $^4\text{He}$  and  $^3\text{He}$  films.

There is also important experimental evidence for structural changes in the second layer from measurements of the heat capacity. Heat capacity maxima are observed arising from the second layer at coverages in the vicinity of where the putative 4/7 phase would occur for both  $^3\text{He}$  and  $^4\text{He}$  films at 1.0K and 1.5K respectively [39, 53]. These maxima, when scaled appropriately, are of similar shape, Fig. S5. This result has been recently extended using a higher quality exfoliated graphite substrate [54], providing evidence for the melting of a new quantum phase.

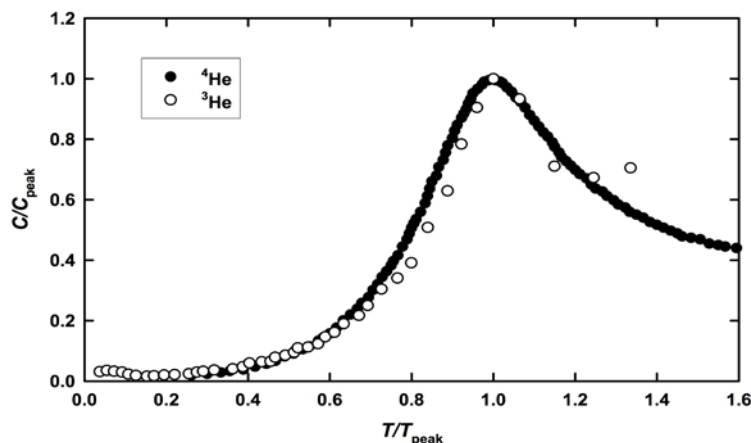


**Fig. S5.** Scaled heat capacity peaks for second layer  $^3\text{He}$  and  $^4\text{He}$ , original data from [40, 53].

We note that any comparison of the results of different experiments requires the alignment of the slightly different coverage scales used by different groups. This also applies to comparison with the results of simulations. Such adjustments are particularly important in the present work, where the anomalous superfluid response is observed over a narrow coverage range preceding promotion to a third layer. In this case it is natural to choose promotion to the third layer as the fiducial point, and we adopt that procedure here. In our case this coverage corresponds to  $20.0 \text{ nm}^{-2}$ , [48, 49]. The details of scaling of the various coverage scales are given in a footnote [50].

In the present torsional oscillator experiment we find clear systematics in the evolution with coverage of the temperature dependence of oscillator dissipation  $Q^{-1}(T)$ , Fig. S9-S12. The dissipation exhibits distinctive maxima. The correlation between the evolution of the temperature of these dissipation maxima and features in the heat capacity, measured by Greywall [53], are shown in Fig. S6.

The evolution of the temperature of dissipation maxima with coverage, over a wider coverage range, is shown in Fig. S7. The systematics of the dissipation data, and the correlation with the superfluid response is discussed in the following.

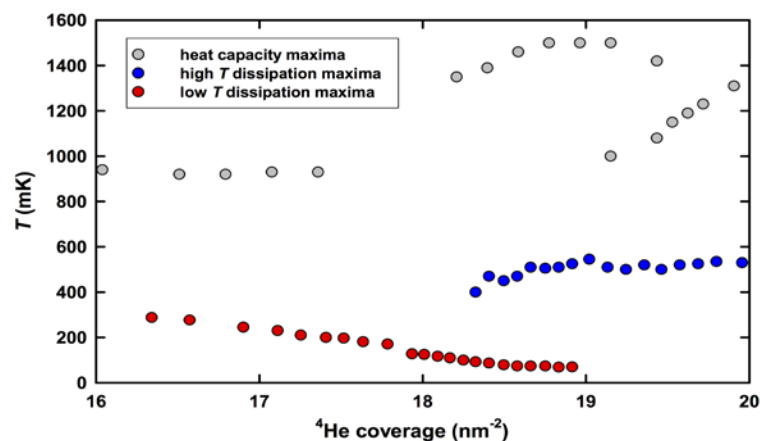


**Fig. S6.** Heat capacity maxima [53], converted to the present coverage scale, and dissipation maxima, as a function of coverage.

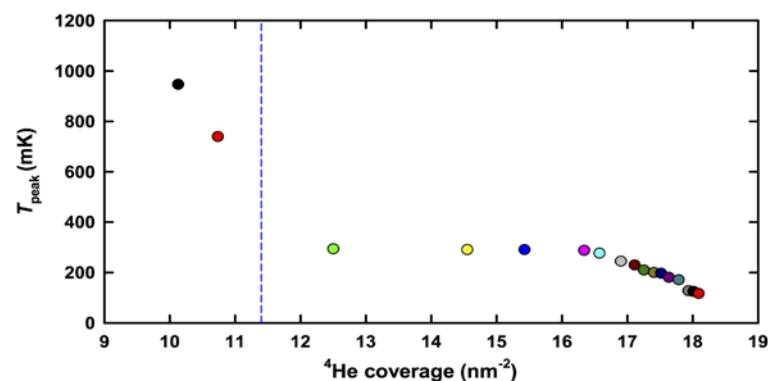


**Fig. S7.** Position of dissipation maxima over range  $10.13 \text{ nm}^{-2}$  to  $18.09 \text{ nm}^{-2}$ . The vertical dashed line indicates layer promotion as determined by a vapour pressure isotherm at 4.2K.

## 2.1 From liquid gas coexistence region to uniform fluid

In the first layer the temperature of the dissipation maximum, Fig. S7, shows a decrease as the first layer density is increased. With the formation of the second layer, a plateau is observed, which we interpret as a signature of the predicted two phase liquid-gas coexistence region, arising from two-dimensional condensation. Thus over the anticipated liquid-gas coexistence region (measured coverages  $12.50$ ,  $14.55$ ,  $15.43$ ,  $16.34 \text{ nm}^{-2}$ ) we observe a maximum in dissipation initially at  $300 \text{ mK}$ , shifting down in temperature only very slightly to  $270 \text{ mK}$  at  $16.34 \text{ nm}^{-2}$ . Over this coverage range the predicted second-layer condensation temperature is  $0.75 \text{ K}$  to  $0.8 \text{ K}$ , so at  $300 \text{ mK}$  the second layer should comprise liquid puddles. We account for the absence of a coverage dependence to the dissipation in this regime as follows. The dissipation maximum at  $0.3 \text{ K}$  is attributed to the viscoelastic response of the exfoliated graphite/helium adsorbate composite system. The submonolayer film data show this to be a strong function of first layer density. In the puddling regime, the first layer density is approximately constant since the spreading pressure of the second layer is zero, and the coverage dependence of the first layer density due to compression by the second layer is negligible. This picture is consistent with neutron scattering measurements of the first layer density [45].

From  $16.57 \text{ nm}^{-2}$  there is a clear onset of coverage dependence to the dissipation data (Fig. S7), that we identify with the end of liquid-gas coexistence and the establishment of a uniform fluid phase.

The result identifies the density of self-bound liquid in the second layer to be  $4.7 \pm 0.1 \text{ nm}^{-2}$ , in good agreement with theoretical predictions [37, 38].

Over the coverage range  $16.57$  to  $17.64 \text{ nm}^{-2}$  we observe a smooth downshift in both the temperature and magnitude of the dissipation maximum, Fig. S8, that we attribute to compression of the first layer due to the increase of the density of the uniform liquid second layer. Within this uniform fluid regime, the coverage  $17.41 \text{ nm}^{-2}$  is the first to show clear evidence of the onset of a frequency shift at low temperature, below 100 mK, which we interpret as mass decoupling due to superfluidity.

This absence of strong superfluid signal at the lowest densities of uniform liquid is consistent with prior observations in the third layer of  $^4\text{He}$  on graphite [46] and the first superfluid layer of  $^4\text{He}$  on graphite pre-plated with two and above atomic layers of hydrogen [47]. These systems display a strong intrinsic coverage-dependent suppression of superfluid density in a fluid layer, which has so far not received a clear explanation. Possible candidates are: the influence of periodic potential due to the solid first helium layer on the superfluid transition of the second layer fluid; influence of proximity to spinodal point of the 2D liquid-gas phase transition.

## 2.2 Transition from uniform fluid to phase with broken translational symmetry

The temperature of the dissipation maximum shows a clear down-step between  $17.78$  and  $17.93 \text{ nm}^{-2}$  from 180 mK to 130 mK, Fig. S7. With subsequent increase in coverage from  $17.93$  to  $18.09 \text{ nm}^{-2}$ , the dissipation maximum displays only a small shift in temperature,  $< 10 \text{ mK}$ , but grows in magnitude, Fig. S9. Over this coverage range the mass-decoupling frequency shift increases more rapidly, with the maximum frequency shift occurring at  $18.09 \text{ nm}^{-2}$ : see frequency shift isotherm Fig. 1F and 2A inset (main body of paper). This leads us to identify the coverage range  $17.78 \pm 0.05$  to  $18.09 \pm 0.05 \text{ nm}^{-2}$  as a narrow two-phase coexistence region, the two phases being fluid and a new phase with broken translational symmetry. The scaling analysis supports a picture of two-phase coexistence over a somewhat wider coverage range, which we denote as region A (see Fig 2A inset and further discussion in section 4).

Thus the raw torsional oscillator data, taken by themselves, refute the most recent theoretical prediction [38] that the second layer fluid remains liquid up to third layer promotion (where incommensurate solid forms).

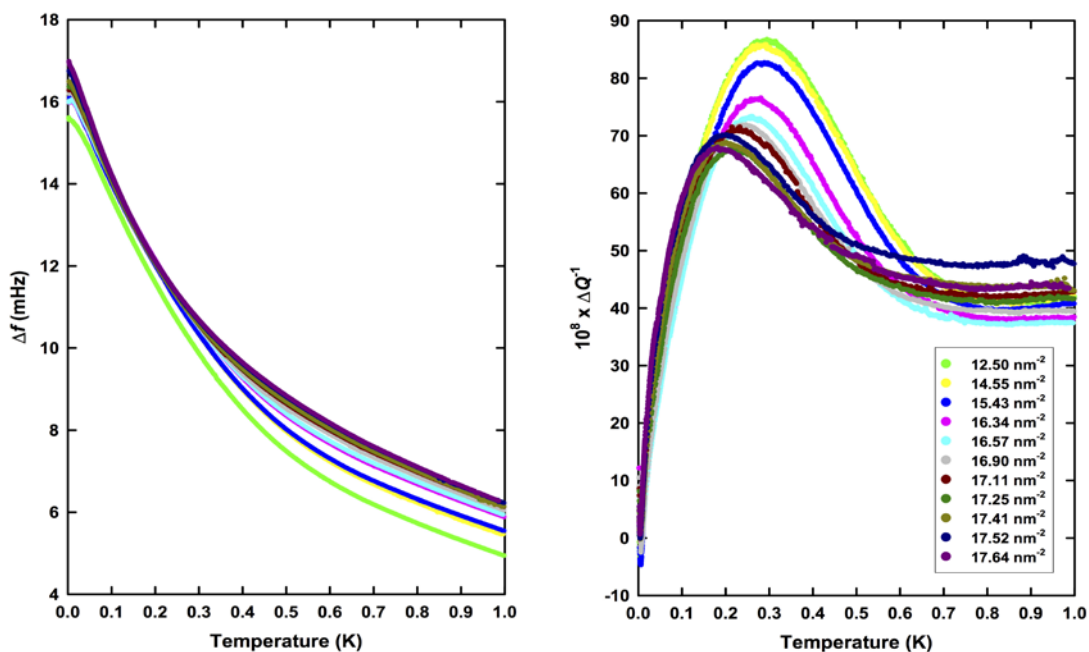
## 2.3 Anomalous superfluid coverage regime

As stated in the previous section the maximum superfluid frequency shift occurs at  $18.09 \text{ nm}^{-2}$ . The height of the dissipation maximum is also greatest at this coverage, which is close to the low temperature coverage-driven transition from uniform liquid to a liquid-solid coexistence predicted by PIMC simulations [37]. This supports the identification of the anomalous superfluid regime, as arising from a film structure with broken translational symmetry. Note, we apply a scaling of the coverages in the theory paper by a factor 0.943; this factor is determined by matching the coverage we experimentally determine for third layer promotion, from our measurements of the heat capacity [49] to the theoretically quoted value.

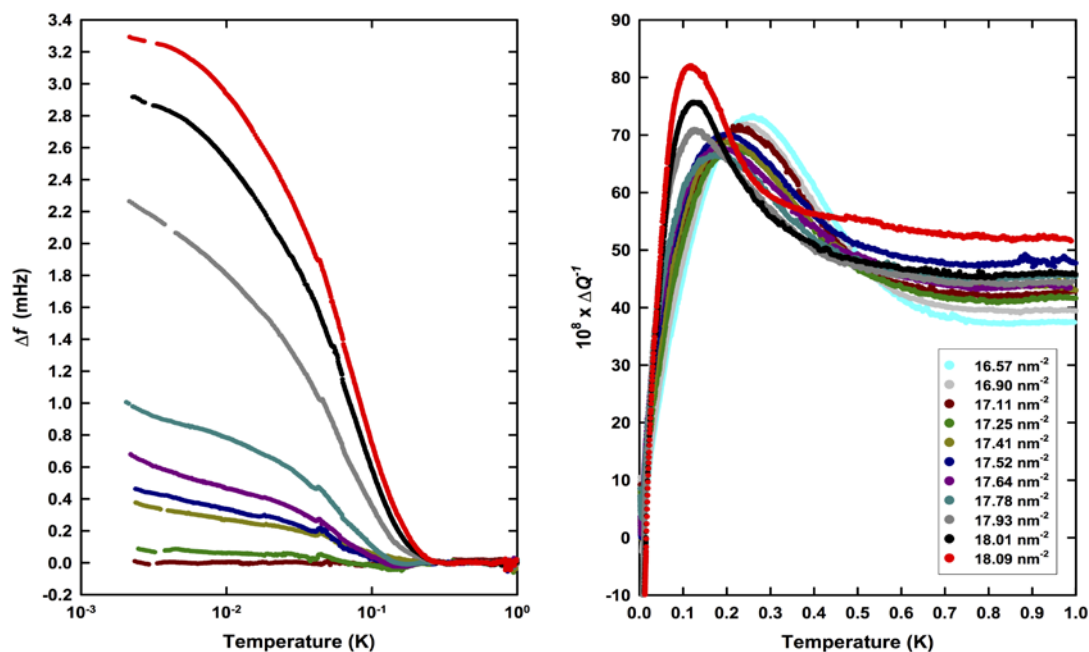
The data from  $18.09 \text{ nm}^{-2}$  to  $19.96 \text{ nm}^{-2}$  are shown in the main body of the paper, and we provide some further commentary here, with information on the dissipation data.

Fig. S10 shows the frequency shift data, after composite background subtraction, and the dissipation data (empty cell background subtracted) for coverages  $18.09 \text{ nm}^{-2}$  to  $19.24 \text{ nm}^{-2}$ . As discussed in more detail in section 4, these correspond to regimes I and II of the scaling analysis, where single parameter collapse is achieved.

On increasing the coverage from  $18.09 \text{ nm}^{-2}$ , we first observe a gradual down shift in the temperature of the dissipation maximum, and reduction in its magnitude, Fig. S10. A new maximum in dissipation at around 0.5 K gradually appears (we first observe a clear maximum at  $18.41 \pm 0.1 \text{ nm}^{-2}$ ), Fig. S11. This is close to the transition from region I to region II scaling discussed in section 4, and may therefore reflect a change in the structure of the second layer.



**Fig. S8.** Frequency shift (empty cell background subtracted and corrected for mass sensitivity) and dissipation (empty cell subtracted) for coverage range between 12.50  $\text{nm}^{-2}$  and 17.64  $\text{nm}^{-2}$ .



**Fig. S9.** Frequency shift (composite background subtracted corrected for mass sensitivity) and dissipation (empty cell subtracted) for coverage range between 16.57  $\text{nm}^{-2}$  and 18.09  $\text{nm}^{-2}$ . Region A extends from 17.25  $\text{nm}^{-2}$  to 18.09  $\text{nm}^{-2}$ .

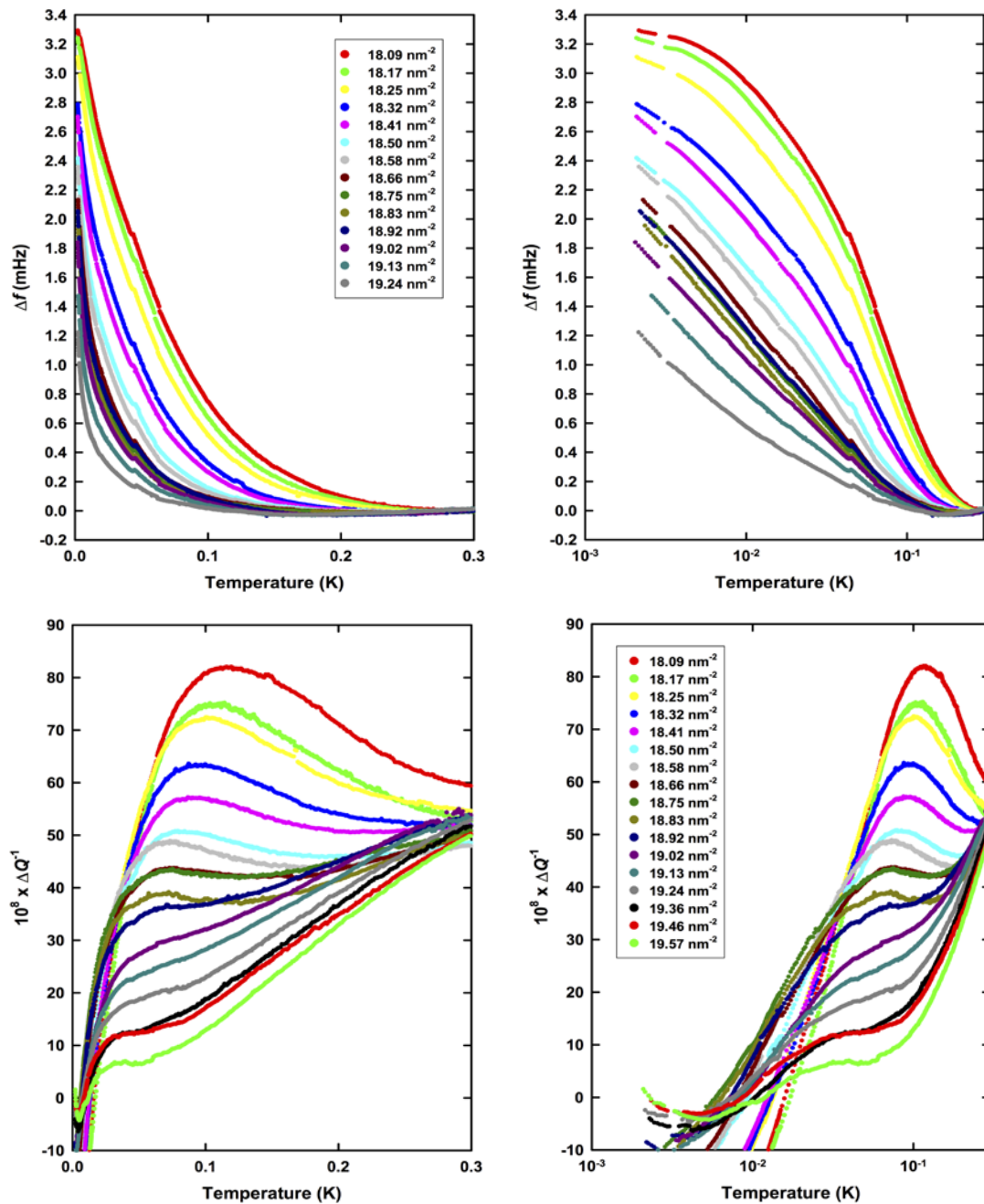


**Fig. S10.** Frequency shift (composite cell background subtracted and corrected for mass sensitivity) and dissipation (empty cell subtracted) for coverage range between 18.09 nm<sup>-2</sup> and 19.24 nm<sup>-2</sup>, regions I and II.

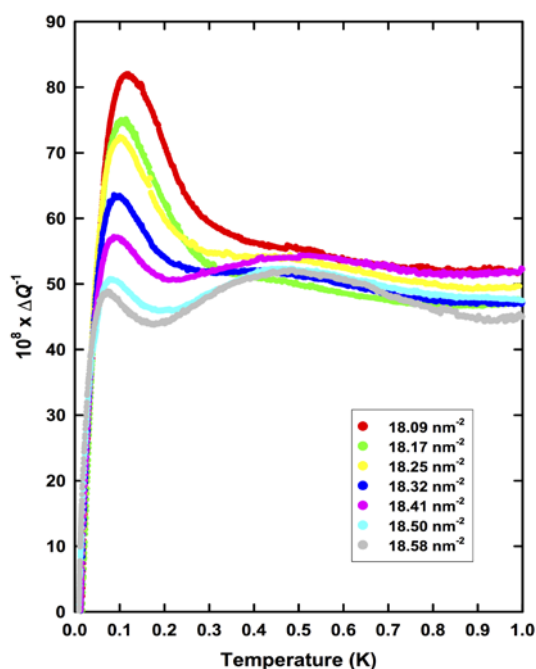


**Fig. S11.** Dissipation (empty cell subtracted) for coverage range between  $18.09 \text{ nm}^{-2}$  and  $18.58 \text{ nm}^{-2}$  showing the evolution of the high temperature dissipation maximum.

Above  $18.41 \text{ nm}^{-2}$  the high temperature dissipation maximum exhibits only a small growth in magnitude, while remaining at a fixed temperature of  $0.5 \text{ K}$ . The low temperature dissipation feature becomes weaker until it is only apparent as a shoulder in  $Q^{-1}(T)$  [51].

In Fig. S12 we show the frequency shift and dissipation data for coverages from  $19.36$  to  $19.96 \text{ nm}^{-2}$ . This is an interval of second layer coverages, prior to third layer promotion, over which single parameter scaling breaks down, labelled regime B. This is indicative of an intervening phase, which interrupts the approach of regime II to the quantum critical point discussed in the main body of the paper. See section 4 for further discussion.

In order to check for critical velocity effects, measurements were made, at the end of the run, at a selection of coverages with a rim velocity of order  $500 \mu\text{ms}^{-1}$ , an order of magnitude greater than that in the main experiment. A comparison of results at two superfluid coverages ( $18.17$  and  $18.83 \text{ nm}^{-2}$ ) with those at two non-superfluid coverages ( $19.96$  and  $20.94 \text{ nm}^{-2}$ ) showed no significant detectable influence of substrate velocity. This procedure makes allowance for the possible dependence of oscillator background on rim velocity.

### 3 Calibration of superfluid density

*In this section we describe the calibration of the superfluid frequency shift data in the anomalous regime by measurements on a known system: the BKT transition in the fluid third layer, atop two solid layers.*

A feature of all studies of superfluid films, as well as superfluidity in porous media, is significant entrainment of the superfluid film arising from substrate connectivity or pore geometry respectively [52]. This effect is parameterised by a  $\chi$ -factor, where  $1 - \chi$  gives the fraction of superfluid that decouples from the surface. It is well established [46] that exfoliated graphite substrate has small  $1 - \chi$  due to the relatively poor connectivity of the substrate over long length scales, comparable to torsional oscillator dimensions. A determination of the  $\chi$ -factor is necessary to convert measurements of the frequency

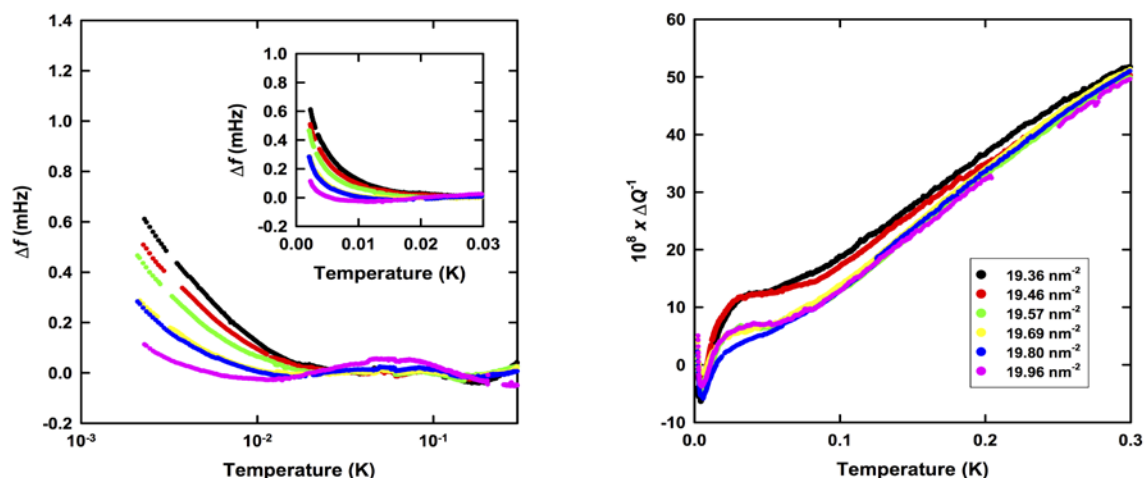


**Fig. S12.** Frequency shift (composite background subtracted corrected for mass sensitivity) and dissipation (empty cell subtracted) for coverage range between  $19.36 \text{ nm}^{-2}$  and  $19.96 \text{ nm}^{-2}$ , close to third layer promotion, region B.

shift to superfluid density. Here we calibrate the superfluid density measurements in the second layer by a measurement of the BKT transition of a thicker  $^4\text{He}$  film, Fig S13. This film had a total coverage of  $26.67 \text{ nm}^{-2}$  corresponding to two solid layers with a fluid overlayer (third layer) of density  $5.5 \text{ nm}^{-2}$ , and is close to fourth layer promotion. From the observed frequency shift of the above superfluid film, and the measured mass loading sensitivity of this oscillator we infer  $\chi = 0.942$ , comparable to values we measured previously with exfoliated graphite substrates prepared using the same heat treatment protocols [47]. Our measured  $1 - \chi$  is significantly larger than the value determined by [46].

A comparison with a range of samples in the second layer, with similar layer density, is shown in Fig S13. It is apparent that at coverage  $18.66 \text{ nm}^{-2}$  the  $T = 0$  superfluid fraction is close to 0.5. Thus the observed superfluid response is essentially a property of the entire second layer. It does not arise from the spontaneous appearance of vacancies by the Andreev-Lifshitz mechanism [55]. Neither can it arise from the hole or interstitial doping of a Mott-insulator commensurate phase.

We now briefly mention the relationship of our experiment with previous and contemporary torsional oscillator experiments on this system. Our results are consistent with the previous work of Crowell and Reppy [46], who first identified an anomalous temperature dependence of the frequency shift over a narrow range of coverages, from  $17.1$  to  $18.5 \text{ nm}^{-2}$  on our scale. Their frequency shift isotherm at a temperature of 20 mK, their lowest temperature, showed the appearance and subsequent apparent disappearance of superfluidity in the second layer. The results of Crowell and Reppy inspired our present measurements to ultralow temperatures. Crowell and Reppy proposed a second layer phase diagram, based on the heat capacity measurements of [53]. This led them to the conclusion that second layer superfluidity is *destroyed* by solidification. Several alternative scenarios were also discussed. However it is important to note that their phase diagram is inconsistent both with subsequent experiment [53, 54] and with theoretical predictions [37], as discussed elsewhere. The coverage at which the maximum frequency shift in the second layer occurs, measured in [46], agrees with our result within  $0.1 \text{ nm}^{-2}$ , after applying the coverage re-scaling described in [50].

A subsequent torsional oscillator experiment, at coverage  $18.7 \text{ nm}^{-2}$  [56], is consistent with the data of [46]. There is no evidence of critical velocity effects up to  $4000 \mu\text{ms}^{-1}$  in [46]. Response as a function of rim velocity was also studied up to  $1050 \mu\text{ms}^{-1}$  at  $18.7 \text{ nm}^{-2}$  in [56], but it is difficult to make definitive conclusions on critical velocity from this data.

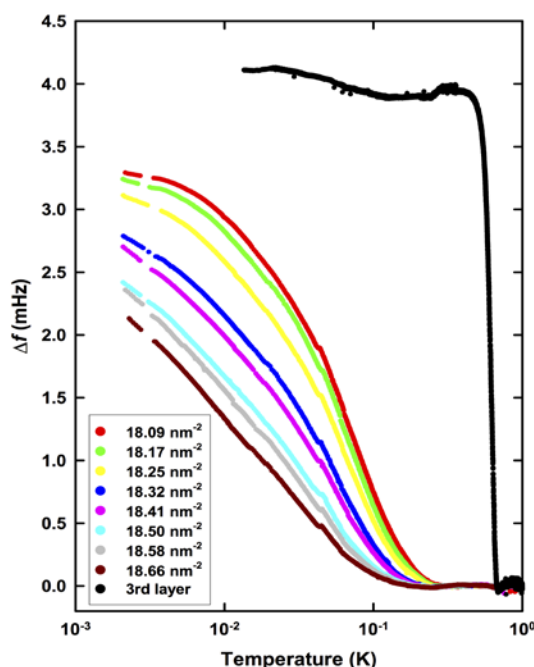


**Fig. S13.** Frequency shift (empty cell background subtracted and corrected for mass sensitivity) for coverage range between  $18.09 \text{ nm}^{-2}$  and  $18.66 \text{ nm}^{-2}$  and third layer sample undergoing the Kosterlitz-Thouless transition.

## 4 Scaling the data

We describe in more detail the procedure used to scale the superfluid density data. Two coverage regimes (I and II) with different single parameter scaling emerge. Scaling in the higher coverage range, regime II demonstrates quantum criticality, as discussed in the paper. Two additional regimes, A and B, displaying two parameter scaling are also discussed.

We seek scaling of the data according to the form  $\frac{\rho_s(T,n)}{\rho} = \frac{\Delta(n)}{T_0} f(T/\Delta(n))$  where  $n$  is the second layer density. Here  $T_0$  is chosen so that  $f(0) = 1$ , and so  $\frac{\rho_s(T=0,n)}{\rho} = \frac{\Delta(n)}{T_0}$ . The superfluid density is then described over a range of coverages by a universal function, with its temperature dependence governed by a single energy scale  $\Delta(n)$ , which depends on layer density. Explicitly the scaling procedure is: plot  $\log \rho_s$  against  $\log T$ ; choose one reference coverage  $n_i$ , let the energy scale parameter for this coverage be  $\Delta(n_i)$ ; apply equal shift ( $\log \alpha$ ) to both  $\log \rho_s$  and  $\log T$  to seek collapse over entire measured temperature range with data at  $n_j$ ; then  $\alpha \Delta(n_j) = \Delta(n_i)$ . This procedure involves no assumption about the form of the function  $f(T/\Delta(n))$ .

The frequency shift data are first converted to  $\rho_s/\rho$ , using the superfluid transition in the third layer as a normalisation, as previously discussed. The second layer density is determined from the total coverage, by subtracting the first layer density; the small compression of the first layer with increasing coverage is accounted for using direct neutron scattering measurements of the first layer density [45].

We find two coverage intervals, referred to as I and II, in which the data collapse with this single parameter scaling.

**Regime I.** We chose  $18.09 \text{ nm}^{-2}$  as our reference coverage. The data at coverages  $18.17$ ,  $18.25$ ,  $18.32$ ,  $18.41 \text{ nm}^{-2}$  collapse onto this reference coverage. By construction  $T_0$  is independent of coverage and  $\Delta$  scales between coverages according to the factors  $\alpha$  determined by the procedure above. The absolute values of  $\Delta$  and  $T_0$  are obtained from fits to the collapsed data. We find that the collapsed

data is well described by  $f(T/\Delta) = 1/(1 + (T/\Delta)^\omega)$ ; the best fit for  $T < \Delta$  is obtained with  $\omega = 1$ . At the reference coverage we find  $\Delta(n = 18.09 \text{ nm}^{-2}) = 43.0 \pm 0.5 \text{ mK}$  and  $T_0 = 53.8 \text{ mK}$ .

**Regime II** Coverages 18.50, 18.58, 18.66, 18.75, 18.83, 18.92, 19.02, 19.13, 19.24  $\text{nm}^{-2}$  collapsed onto the chosen reference coverage 18.66  $\text{nm}^{-2}$ . We find  $f(T/\Delta) = 1/(1 + T/\Delta)$  fits the data well up to  $T/\Delta \sim 4$ . The absolute values of  $\Delta$  and  $T_0$  are obtained from fits to the collapsed data. We obtain  $\Delta(n = 18.66 \text{ nm}^{-2}) = 10.9 \pm 0.2 \text{ mK}$  and  $T_0 = 21.5 \text{ mK}$ .

Together with the factors  $\alpha$  determined by these scalings, this generates the absolute values shown in Fig. 2 (c). We emphasize that the relative scaling of the  $\Delta(n)$  shown there is independent of the fit to the temperature dependence. To leading order  $\frac{\rho_s(T,n)}{\rho} = \frac{\rho_s(0,n)}{\rho} - \frac{T}{T_0}$ .

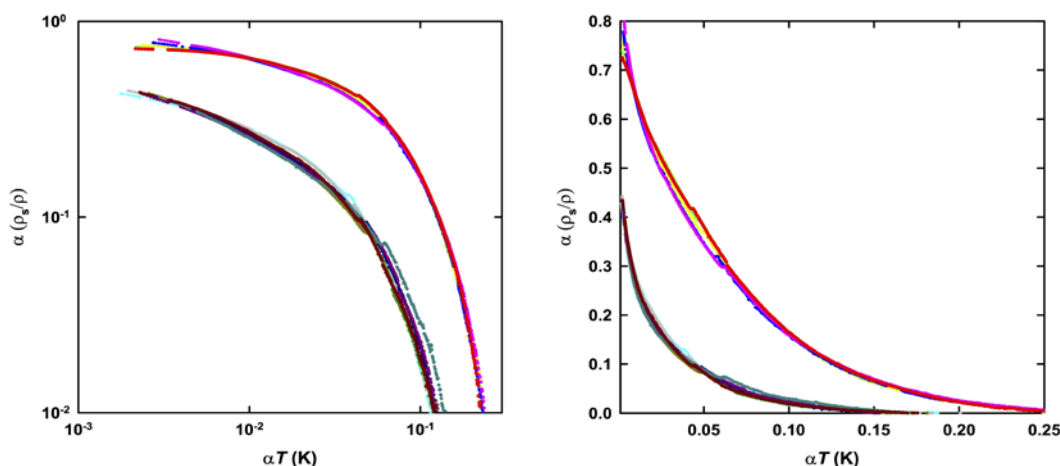


**Fig. S14.** The two regimes of data collapse. Regime I: upper curve. Regime II: lower curve.

The data collapse onto the two reference coverages, specified above, is shown in Fig. S14. Fig. 2 of the main body of the paper shows most clearly the difference of the two functional forms in regime I and II, which deviate for  $T > \Delta$ . The two regimes show a different coverage dependence of  $\Delta$  as well as different values of  $T_0$ , Fig 2C. These two distinct coverage ranges of collapse support our proposal that the anomalous superfluidity arises from the simultaneous breaking of translational symmetry, suggesting distinct spatial structure in regimes I and II. The border of these two regimes is correlated with the appearance of a new weak dissipation maximum at 0.5 K, Fig S11.

In the main body of the paper we argue that regime II corresponds to superfluidity with incommensurate density wave order. The structure factor in regime I is expected to be different, but still incorporating some form of density wave order, perhaps liquid-crystal like.

**Regimes A and B** The data in coverage ranges A and B do not collapse with single parameter scaling. Regime A: Coverages 17.25, 17.41, 1.52, 17.64, 17.78, 17.93, 18.01, 18.09  $\text{nm}^{-2}$ . Regime B: Coverages 19.36, 19.46, 19.57, 19.69, 19.80, 19.96  $\text{nm}^{-2}$ .

However collapse was achieved with two separate scaling factors for the superfluid density and temperature axis, shown in Fig. S15, according to  $\alpha_\rho \frac{\rho_s}{\rho} = A f\left(\frac{\alpha_T T}{\Delta}\right)$ .

The behaviour in regimes A and B differs. In the regime A the scaling factor for the temperature axis shows no strong coverage dependence, while that for the superfluid density axis shows a marked increase. This is suggestive of a two phase coexistence over this narrow coverage range between non-superfluid and superfluid components, the fraction of the latter increasing with increasing coverage. In regime B, the scaling shows only a relatively small decrease up to layer promotion of the  $T = 0$  superfluid density. However the characteristic energy (or equivalently characteristic temperature below which superfluidity gradually appears) decreases approximately linearly with coverage towards zero at layer promotion. More detailed studies at low mK temperatures, coupled with improved knowledge

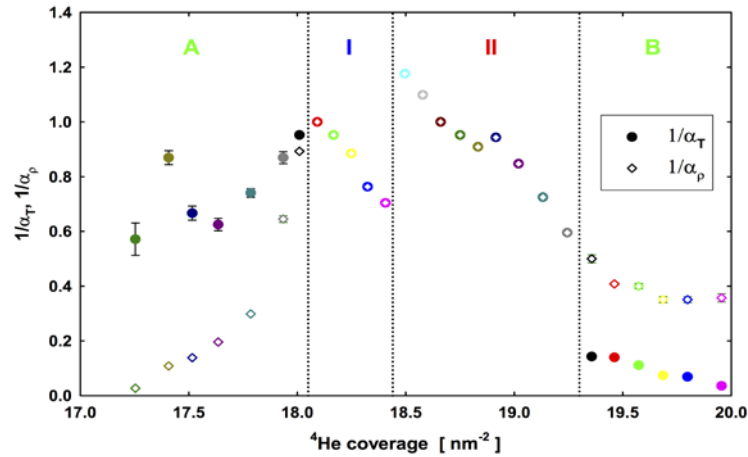


**Fig. S15.** Scaling parameters as a function of coverage. Vertical dotted lines show coverage boundaries which mark transition between different scaling regimes. Regime I and II display different single parameter scaling. Regimes A and B show two parameter scaling of different forms.

of the background and of film structure, are desirable, but challenging. Nevertheless, this result suggests the tantalising possibility that, superfluid response survives up to layer completion, but with a vanishing temperature onset.

## 5 Superfluid density from excitation spectrum ansatz.

We can account for the leading order temperature dependence of the superfluid density via an ansatz for the elementary excitation spectrum, consistent with incipient density wave ordering.

The superfluid density  $\rho_s$  relates the supercurrent  $\mathbf{j}_s$  to the superfluid velocity  $\mathbf{v}_s$ ,

$$\mathbf{j}_s = \rho_s \mathbf{v}_s. \quad (1)$$

At a finite temperature, thermally excited quasiparticles deplete the superfluid so that

$$\rho_s(T) = \rho_s(0) - \rho_n(T) \quad (2)$$

where  $\rho_s(0)$  is the ground-state superfluid density and  $\rho_n(T)$  is the thermal depletion of the superfluid density. This quantity is determined by the momentum stress tensor of the quasiparticle fluid, given by the Landau formula [57]

$$\rho_n \delta_{ij} = - \int \frac{d^d \mathbf{p}}{(2\pi\hbar)^d} p_i p_j \frac{\partial}{\partial E_{\mathbf{p}}} \left( \frac{1}{\exp(E_{\mathbf{p}}/k_B T) - 1} \right) \quad (3)$$

where  $p_i$  is the momentum in the  $i$  direction,  $d$  is the dimensionality,  $T$  the temperature and  $E_{\mathbf{p}}$  is the energy of a quasiparticle with momentum  $\mathbf{p}$  and we have assumed an isotropic superfluid response. For a conventional superfluid with a linear phonon spectrum,  $E_{\mathbf{p}} = v|\mathbf{p}|$ , this gives a low-temperature dependence of  $\rho_n \propto T^{d+1}$ . One can derive this result heuristically by noting that for linear dispersion, momentum and energy have the same dimension, and that the dimensionality of the integral is  $[E^{d+1}] \sim T^{d+1}$ . Note that at low temperatures, the momentum of the excitations vanishes linearly with temperature, because the dispersion is centered at zero. In two dimensions, this gives rise to a  $T^3$  reduction to the superfluid density with increasing temperature preceding the BKT transition, as has previously been observed in experiments on superfluid  $^4\text{He}$  films on hydrogen preplated graphite [47].

The linear- $T$  drop in the superfluid response at low temperatures found in second layer  $^4\text{He}$  implies a much more rapid depletion of the superfluid density which is most naturally attributed to the excitation of high-momentum quasiparticles, centered around a set of ordering wavevectors  $\hbar\mathbf{G}$  with dispersion

$$E_{\mathbf{p}} \sim c|\mathbf{p} - \hbar\mathbf{G}| \quad (4)$$

where  $c$  is the sound speed. We interpret this as a consequence of an incipient density wave ordering at the wavevectors  $\mathbf{G}$ . Finite temperatures now excite cones of high-momentum excitations centered around  $\mathbf{p} \sim \hbar\mathbf{G}$ . Since the characteristic momentum of the excitations is finite at low temperatures, the depletion of the superfluid density is qualitatively larger. In keeping with this logic, we see that the momentum product  $p_i p_j \sim [\mathbf{G}]_i [\mathbf{G}]_j$  in (3) can be factored out of the stress momentum integral at low temperatures so that

$$\rho_n \delta_{ij} \sim - \sum_{\mathbf{G}} G_i G_j \int \frac{d^d \mathbf{p}}{(2\pi\hbar)^d} \frac{\partial}{\partial E_{\mathbf{p}}} \left( \frac{1}{\exp(E_{\mathbf{p}}/k_B T) - 1} \right). \quad (5)$$

This factorization reduces the dimension of the stress momentum integral by two,  $[\rho_n] \sim T^{d-1}$  so the high momentum of the quasiparticles leads to a linear reduction of the superfluid condensate in  $d = 2$ .

We now carry out a more detailed calculation of the quasiparticle depletion of a modulated superfluid. Supposing a 2D triangular lattice in real space, then on symmetry grounds, the soft-modes will be located at the six density wave ordering wavevectors.

$$\mathbf{G} \in \{\pm G(1, 0), \pm G(1/2, \sqrt{3}/2), \pm G(-1/2, \sqrt{3}/2)\} \quad (6)$$

as shown in Fig. S16. Here the magnitude  $G = 2\pi/(a \cos 30^\circ) = 4\pi/(a\sqrt{3})$  corresponds to a triangular lattice of side length  $a$ .

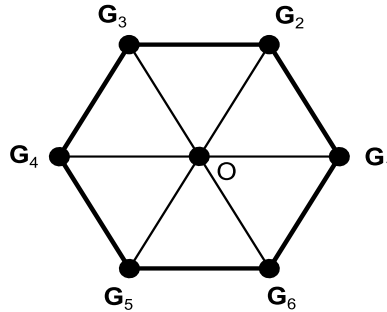


**Fig. S16.** Star of vectors  $\mathbf{G}_{1,2,\dots,6}$  showing location of gapless rotons. The vectors  $\mathbf{G}$  are incommensurate, but are aligned with the underlying triangular lattice substrate

To carry out the calculation of the superfluid stiffness, we approximate the dispersion relation around each  $\mathbf{G}$  by:

$$E_{\mathbf{p} \simeq \hbar\mathbf{G}} = [E_0^2 + c^2(\mathbf{p} - \hbar\mathbf{G})^2]^{1/2}. \quad (7)$$

We have introduced a small roton-like gap  $E_0$ . This might be an intrinsic property of the system or it may arise as a consequence of the finite domain size of the modulated superfluid. Such domains can arise from a variety of effects, including the finite experimental cell and the platelet size of the underlying graphite substrate.

The leading low-temperature contribution to  $\rho_n$  from the excitations near  $\mathbf{G}$  is given by

$$\begin{aligned} \rho_n(T) &\simeq \sum_{\mathbf{G}} \frac{(\hbar G)^2}{k_B T} \int \frac{d^2 \mathbf{p}}{(2\pi\hbar)^2} \frac{(E_0^2 + c^2 \mathbf{p}^2)^{1/2}}{\left[ e^{(E_0^2 + c^2 \mathbf{p}^2)^{1/2}/k_B T} - 1 \right]^2} \\ &= \frac{3G^2 k_B T}{\pi c^2} \int_{E_0/k_B T}^{\infty} \frac{x e^x dx}{(e^x - 1)^2} \end{aligned} \quad (8)$$

where we have taken the upper cutoff to infinity because we believe that we have reached temperatures below the bandwidth of the excitation spectrum. This gives a  $T \ln T$  contribution to the fractional normal density:

$$\frac{\rho_n}{\rho} = \left( \frac{4\sqrt{3}\pi}{m_4 c^2} \right) k_B T \left( 1 + \ln \left( \frac{k_B T}{E_0} \right) \right), \quad (9)$$

where  $\rho = 2m_4/\sqrt{3}a^2$  is the total mass density,  $m_4$  is the mass of the helium atom and we have used  $Ga = 4\pi/\sqrt{3}$ .

Within the range of temperature in our experiments, the logarithmic term varies slowly, giving rise to a dominant linear temperature dependence. From our results, we can extract  $\rho_n/\rho = [\rho_s(0) - \rho_s(T)]/\rho \simeq T/T_0 + O(T^2)$  where  $T_0 = 21.5$  mK, in regime II. Comparing with (9), we find that  $c \simeq [1 + \ln(k_B T/E_0)]^{1/2} \times 31$  m/s.

We can also comment on the ordering wavevector  $\mathbf{G}$  as a function of coverage. The experiment suggests that  $\partial(\rho_s/\rho)/\partial T|_{T=0} = -1/T_0$  is independent of coverage  $n$ . On the other hand, Eq. (9) suggests  $\partial(\rho_s/\rho)/\partial T|_{T=0} \propto (Ga)^2/c^2$  at fixed temperature. Assuming that  $c^2$  does not change significantly with coverage, we come to the conclusion that  $G^2$  for the density wave is proportional to the second-layer coverage  $\sim 1/a^2$ . In other words, the system has a density wave order that is *incommensurate* with the underlying substrate and first helium layer.

On finite size effects: note that superfluidity would be lost at finite temperatures if the excitations at momentum  $\hbar\mathbf{G}$  were truly gapless ( $E_0 \rightarrow 0$ ). Generally, for intrinsic and finite-size gap contributions we would have

$$E_0 = \sqrt{E_{\text{in}}^2 + (c\hbar/L)^2} \quad (10)$$

where  $E_{\text{in}}$  is the intrinsic gap and  $L$  is the large-distance cutoff. The present experiment cannot distinguish between an intrinsic gap and finite size effects.

The inferred value of the effective speed which enters the dispersion relation is only weakly dependent on finite size. The magnitude of the roton-like gap also determines the Landau critical velocity. The observed lower bound on the critical velocity of around  $1 \text{ mms}^{-1}$  implies a lower bound on the effective roton gap of order  $0.1$  mK. If this gap were to arise solely from finite size, this would place an upper bound on platelet size of  $5 \mu\text{m}$ . This is two orders of magnitude larger than the crystallite size we determined by analysis of x-ray diffraction from a similar exfoliated graphite sample [58]. It is important to note that torsional oscillator measurements of the superfluid density rely on the connectivity of flow path over the dimensions of the entire sample. This connectivity is parameterised by the  $\chi$  factor discussed in section 3.

## 6 Trial wavefunction for intertwined superfluid and density wave order

The ground state of a superfluid with density wave order should exhibit simultaneous condensation of the bosons at zero momentum with a complex order parameter

$$\langle b_{\mathbf{q}=0} \rangle = \alpha_0, \quad (11)$$

together with the development of a density wave order parameter at the characteristic modulation wavevectors  $\mathbf{G}$ ,

$$\langle \hat{\rho}_{\mathbf{q}=\mathbf{G}} \rangle = \rho_{\mathbf{G}}. \quad (12)$$

The density operator can be expanded in terms of boson creation and annihilation operators:  $\hat{\rho}_{\mathbf{G}} = \sum_{\mathbf{k}} b_{\mathbf{k}-\mathbf{G}}^\dagger b_{\mathbf{k}}$ . Macroscopic occupation of the zero momentum state means that we may use the Bogolyubov substitution, replacing the operators  $b_{\mathbf{k}=0}$  and  $b_{\mathbf{k}=0}^\dagger$  by the numbers  $\alpha_0$  and  $\bar{\alpha}_0$  ( $\bar{\alpha}_0$  is the complex conjugate of  $\alpha_0$ ). Then the dominant (ground state) contribution to the density operator is

$$\hat{\rho}_{\mathbf{G}} = \alpha_0 b_{-\mathbf{G}}^\dagger + \bar{\alpha}_0 b_{\mathbf{G}}. \quad (13)$$

Hence the presence of a finite  $\langle \hat{\rho}_{\mathbf{G}} \rangle$  implies the existence of a condensate component at finite momentum,  $\langle b_{\mathbf{G}} \rangle = \alpha_{\mathbf{G}}$ .

A simple illustrative example of this is the case of a single characteristic modulation wavevector, with condensation into two states, of momentum 0 and  $\mathbf{G}$ . This referred to in the main body of the paper, see Fig 3C. The intertwined ground state will be a linear combination of these two states and it may be represented in terms of the Bloch sphere shown, with the general state given by

$$|\psi\rangle = \left[ \cos \frac{\theta}{2} |0\rangle + e^{i\varphi} \sin \frac{\theta}{2} |\mathbf{G}\rangle \right] e^{i\mathbf{x}}. \quad (14)$$

This corresponds to a wave-function  $\psi(\mathbf{x}) = \langle \mathbf{x} | \psi \rangle$ :

$$\psi(\mathbf{x}) = \left[ \cos \frac{\theta}{2} \psi_0 + e^{i\varphi} \sin \frac{\theta}{2} \psi_{\mathbf{G}}(\mathbf{x}) \right] e^{i\mathbf{x}} \quad (15)$$

where  $\psi_0 = \langle \mathbf{x} | 0 \rangle$ ,  $\psi_{\mathbf{G}}(\mathbf{x}) = \langle \mathbf{x} | \mathbf{G} \rangle$ , and we note that  $\psi_{\mathbf{G}}(\mathbf{x}) \sim e^{i\mathbf{G}\cdot\mathbf{x}} \psi_0$ . At the north pole ( $\theta = 0$ ), we have  $|\psi(\mathbf{x})|^2 = |\psi_0|^2$ , corresponding to a uniform density. At the south pole ( $\theta = \pi$ ) we have  $|\psi(\mathbf{x})|^2 = |\psi_{\mathbf{G}}(\mathbf{x})|^2$ , again corresponding to a uniform density. However in the general case

$$|\psi(\mathbf{x})|^2 = \cos^2 \frac{\theta}{2} |\psi_0|^2 + \sin^2 \frac{\theta}{2} |\psi_{\mathbf{G}}|^2 + \frac{1}{2} \sin \theta [ e^{i\varphi} \psi_0(\mathbf{x})^* \psi_{\mathbf{G}}(\mathbf{x}) + \text{c.c.} ] . \quad (16)$$

Now, in addition to the uniform terms, there is an interference term so that

$$|\psi(\mathbf{x})|^2 \sim 1 + c \sin \theta \cos(\mathbf{G}\cdot\mathbf{x} + \varphi) . \quad (17)$$

Thus in terms of the Bloch sphere, the north pole corresponds to the  $\mathbf{q} = 0$  state alone, with uniform density. The south pole corresponds to the  $\mathbf{q} = \mathbf{G}$  state alone, with uniform density. These are ‘singular’ points. Elsewhere on the sphere there is quantum interference between the  $\mathbf{q} = 0$  and the  $\mathbf{q} = \mathbf{G}$  states, resulting in a density wave of wave vector  $\mathbf{G}$ . The magnitude of this wave is maximal around the equator, going to zero at the poles.

The Bloch sphere picture can only treat a single nonzero ordering wavevector. The simplest class of many-body wavefunction exhibiting intertwined order, with a number of ordering wavevectors is a coherent state

$$|\Psi\rangle = \exp \left( \alpha_0 b_{\mathbf{q}=0}^\dagger + \sum_{\mathbf{G}} \alpha_{\mathbf{G}} b_{\mathbf{G}}^\dagger \right) |0\rangle \quad (18)$$

where  $|0\rangle$  is the vacuum, and  $\mathbf{G}$  is the sextet of ordering wavevectors defined in the previous section (Eq. 6). This coherent state is the eigenstate of the seven boson operators  $b_{\mathbf{q}=0}$  and  $b_{\mathbf{G}}$ , such that

$$b_{\mathbf{q}=0} |\Psi\rangle = \alpha_0 |\Psi\rangle, \quad b_{\mathbf{G}} |\Psi\rangle = \alpha_{\mathbf{G}} |\Psi\rangle. \quad (19)$$

This coherent state is also an eigenstate of the real-space boson field operators,

$$\hat{\psi}(\mathbf{x}) = \frac{1}{\sqrt{L^d}} \sum_{\mathbf{q}} b_{\mathbf{q}} e^{i\mathbf{q}\cdot\mathbf{x}}, \quad (d = 2) \quad (20)$$

such that

$$\hat{\psi}(\mathbf{x}) |\Psi\rangle = \psi(\mathbf{x}) |\Psi\rangle \quad (21)$$

where

$$\psi(\mathbf{x}) = \frac{1}{\sqrt{L^2}} \left( \alpha_0 + \sum_{\mathbf{G}} \alpha_{\mathbf{G}} e^{i\mathbf{G}\cdot\mathbf{x}} \right) \quad (22)$$

is the condensate wavefunction of the modulated superfluid.

The expectation value of the total number  $N$  of bosons in the condensate is

$$N = \langle \hat{N} \rangle = |\alpha_0|^2 + \sum_{\mathbf{G}} |\alpha_{\mathbf{G}}|^2 . \quad (23)$$

As this coherent state (18) is not an eigenstate of the number operator  $\hat{N}$ , it has root-mean-square number fluctuations  $[\langle(\hat{N} - N)^2\rangle]^{1/2}/\langle\hat{N}\rangle \sim 1/\sqrt{N}$  which becomes negligible in the thermodynamic limit.

On the other hand, the Fourier component of the density modulation at wavevector  $\mathbf{Q}$  in this coherent state is given by

$$\langle\Psi|\hat{\rho}_{\mathbf{Q}}|\Psi\rangle = \sum_{\mathbf{k}=0,\mathbf{G}} \bar{\alpha}_{\mathbf{k}-\mathbf{Q}} \alpha_{\mathbf{k}}, \quad (24)$$

where  $\alpha_{\mathbf{p}} = 0$  unless  $\mathbf{p} = 0$  or  $\mathbf{G}$ . In this model wavefunction, the correlation function of the field operators exhibits modulated long-range order. After averaging over the centre of mass coordinate,

$$\int d^2\mathbf{X} \langle\Psi|\hat{\psi}^\dagger(\mathbf{X} + \mathbf{x})\hat{\psi}(\mathbf{X})|\Psi\rangle = |\alpha_0|^2 + \sum_{\mathbf{G}\neq 0} |\alpha_{\mathbf{G}}|^2 e^{i\mathbf{G}\cdot\mathbf{x}}. \quad (25)$$

## 7 Non Abelian Manifold

*We show that our proposed quasi-condensate wavefunction has non Abelian symmetry. Consequently there are no topologically stable defects and the system does not support a finite temperature vortex unbinding BKT transition, as observed.*

In a conventional two dimensional superfluid, the finite temperature superfluid stiffness jumps to zero at the transition temperature. Such transitions are a universal property of x-y type order parameters, and are associated with the unbinding of superfluid vortices at the ‘‘Berezinskii Kosterlitz Thouless’’ (BKT) phase transition.

One of the key observations of our experiment, is the absence of a finite temperature BKT transition. Such transitions are clearly visible in three layer  $^4\text{He}$  films, but are absent in the second layer of  $^4\text{He}$  on graphite investigated here. The absence of a finite temperature BKT transition is remarkable, and indicates that the underlying modulated condensate is unable to support topologically stable vortices. Mathematically, the topologically stable configurations of an order parameter are set by the homotopy classes of the the order parameter manifold. Here we show that a modulated superfluid wavefunction introduced in the last section transforms under a set of non-Abelian operators, generating a homotopy class that does not support stable topological vortices.

To discuss the manifold of low-energy states of this system, we need to discuss its symmetries. In a conventional superfluid, the energy of the system is invariant to a global U(1) phase shift to the condensate wavefunction:

$$\psi(\mathbf{r}) \rightarrow e^{i\phi}\psi(\mathbf{r}), \quad (26)$$

*i.e.*  $\alpha_0 \rightarrow \alpha_0 e^{i\phi}$  and  $\alpha_{\mathbf{G}} \rightarrow \alpha_{\mathbf{G}} e^{i\phi}$  in (22). The system spontaneously breaks this U(1) symmetry by picking a specific global phase. It can be shown that we can write this phase shift as a unitary operation  $\hat{U}_\phi$  on the state  $|\Psi\rangle$ :

$$|\Psi\rangle \rightarrow \hat{U}_\phi|\Psi\rangle = \exp(i\phi\hat{N})|\Psi\rangle, \quad \hat{N} = b_0^\dagger b_0 + \sum_{\mathbf{G}} b_{\mathbf{G}}^\dagger b_{\mathbf{G}} \quad (27)$$

where  $\hat{N}$  is the total boson number operator. At the microscopic level, we expect the Hamiltonian to conserve the number of bosons such that  $\hat{H}$  commutes with  $\hat{N}$ ,  $[\hat{H}, \hat{N}] = 0$ . In turn, this implies that  $\hat{H}$  commutes with  $\hat{U}_\phi$ ,  $[\hat{H}, \hat{U}_\phi] = 0$ , so that  $|\Psi\rangle$  and  $\hat{U}_\phi|\Psi\rangle$  have the same energy.

Since we have a density wave that is incommensurate with the underlying substrate, we also expect that it does not cost energy to translate it in the plane of the helium film. For a translation of  $\delta\mathbf{r} = \mathbf{ln}$ , the density profile changes  $\rho(\mathbf{r}) \rightarrow \rho(\mathbf{r} + \mathbf{ln})$  or  $\rho_{\mathbf{G}} \rightarrow \rho_{\mathbf{G}} e^{i\mathbf{l}\mathbf{G}\cdot\mathbf{n}}$  for the Fourier components. In terms of the coherent state (18), we see from equation (24) that this global translation is achieved by phase shifts in the amplitudes  $\alpha_{\mathbf{G}} \rightarrow \alpha_{\mathbf{G}} e^{i\mathbf{l}\mathbf{G}\cdot\mathbf{n}}$ . This is equivalent to another unitary operation on  $\Psi$ :

$$|\Psi\rangle \rightarrow \exp(i\mathbf{l}\hat{T}_{\mathbf{n}})|\Psi\rangle, \quad \hat{T}_{\mathbf{n}} = \sum_{\mathbf{G}} (\mathbf{G} \cdot \mathbf{n}) b_{\mathbf{G}}^\dagger b_{\mathbf{G}} \quad (28)$$

so  $l\hat{T}_{\mathbf{n}}$  generates translations of length  $l$  in direction  $\mathbf{n}$ . Using the same reasoning as above for the global phase shift, we expect that the translation generators also commute with the Hamiltonian:  $[\hat{H}, \hat{T}_{\mathbf{n}}] = 0$ .

Since  $\hat{N}$  commutes with  $\hat{T}_{\mathbf{n}}$ , the two symmetry operations of global phase shift and global translation commute with each other. However, we must also consider the ‘‘Umklapp operators’’ which excite a quasiparticle between the seven zero modes

$$\begin{aligned}\hat{S}_{0\mathbf{G}} &= b_0^\dagger b_{\mathbf{G}}, & \hat{S}_{\mathbf{G}0} &= b_{\mathbf{G}}^\dagger b_0, \\ \hat{S}_{\mathbf{G}\mathbf{G}'} &= b_{\mathbf{G}}^\dagger b_{\mathbf{G}'} & (\mathbf{G}' \neq \mathbf{G})\end{aligned}\quad (29)$$

where  $\mathbf{G}$  and  $\mathbf{G}' = \mathbf{G}_{1,\dots,6}$ . These operators do not commute, introducing a non-Abelian group symmetry. We shall use the short-hand notation  $\hat{S}_{\alpha\beta} \equiv \hat{S}_{\mathbf{G}_\alpha\mathbf{G}_\beta}$ , ( $\alpha, \beta \in \{0, 1 \dots 7\}$ ) identifying  $\mathbf{G}_0 = (0, 0)$  with the origin. From our interpretation of the linear- $T$  reduction in superfluid density as the existence of almost gapless modes at momenta  $\hbar\mathbf{G}$ , we deduce that the Umklapp processes are zero energy processes that commute with the Hamiltonian,

$$[\hat{H}, \hat{S}_{\alpha\beta}] = 0, \quad (30)$$

forming a larger manifold of degenerate states. *This is the key conjecture of this non-Abelian scenario.*

The important point to note here, is that the the Umklapp and translation operators do not mutually commute, forming a set of *non-Abelian* zero modes defined by the algebra

$$[\hat{S}_{lm}, \hat{S}_{np}] = \delta_{mn}\hat{S}_{lp} - \delta_{lp}\hat{S}_{nm}. \quad (31)$$

The enlarged manifold of states  $\mathcal{M}$  radically changes the topological properties of the modulated superfluid.

The superfluid BKT transition involves vortex unbinding. Vortices are topologically stable point defects, for which there is no continuous deformation of the order parameter that unwinds the vortex. The theory of topological defects classifies them in terms of homotopy classes [59]: point defects are

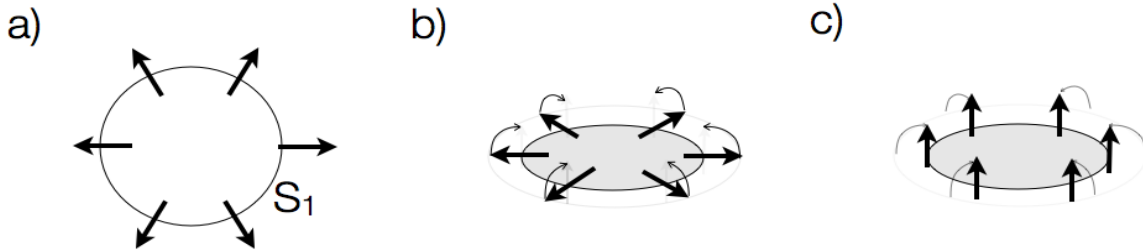


**Fig. S17.** Configuration (a) depicts a vortex configuration of  $O(2)$  planar spins on a closed loop  $S^1$ ; Configuration (b) is a vortex configuration of  $SO(3)$  (Heisenberg) spins on a closed loop. Rotating spins into the  $z$  direction give configuration (c) which has no vortices.

described by mappings of the order parameter manifold  $\mathcal{M}$  onto a closed loop, determined by the first homotopy class  $\pi_1(\mathcal{M})$ . For conventional superfluids, with a single  $U(1)$  phase, the order parameter manifold  $\mathcal{M}$  is a ring  $S^1$  for which  $\pi_1(\mathcal{M}) = \pi_1(S^1) = \mathbb{Z}$ , corresponding to the set of integer winding numbers of vortices. By contrast, for a Heisenberg ferromagnet with the non-Abelian group manifold of  $\mathcal{M} = SO(3)/SO(2) \equiv SU(2)/SU(1)$ ,

$$\pi_1(SO(3)/SO(2)) = 0 \quad (32)$$

expressing the fact that there are no topologically stable vortices. An analogous situation occurs in the modulated superfluid, where the first homotopy class

$$\pi_1(SU(7)/SU(6)) = 0, \quad (33)$$

is empty, implying there no point defects; like a Heisenberg ferromagnet, any vortex configurations which develop can unwind in the third dimension, eliminating the BKT transition.

## 8 Quantum transition

*We identify a quantum phase transition at which superfluidity vanishes. The behaviour is consistent with the Bose-Hubbard universality class.*

We envisage that, as the coverage increases, the density modulations increase in amplitude. This modulated superfluid still has larger number fluctuations than a conventional solid. In a coherent state, the number-phase uncertainty is minimized:  $\Delta N \Delta \phi \sim 1$  with  $\Delta N \propto \sqrt{N}$  and  $\Delta \phi \sim 1/\sqrt{N}$ . Unlike an insulating solid, there is an additional uncertainty in the density associated with the formation of a condensate with a well-defined phase. As the coverage is increased, the compressibility of the system reduces. It decreases the number fluctuations in each local region of the system. The number-phase uncertainty principle dictates that there are increased phase fluctuations at long wavelengths. The zero-momentum condensate will suffer from these quantum phase fluctuations. The superfluidity is lost when phase fluctuations become of order unity. This loss of superfluidity by phase fluctuations is believed to be the mechanism for the superfluid-Mott insulator transition in the Bose-Hubbard model. Our system has more zero modes than such a lattice model, so the analogy should be treated with caution.

The Bose-Hubbard model predicts scaling [7]

$$\rho_s(T, \delta) \approx \delta^{\nu(d+z-2)} F\left(\frac{T}{\delta^{\nu z}}\right) \quad (34)$$

where the coherence length and characteristic energy, governing spatial and temporal fluctuations approaching a QCP, follow  $\xi \approx \delta^{-\nu}$  and  $\Omega \approx \xi^{-z} \approx \delta^{z\nu}$ , where  $\delta$  is the tuning parameter. In our scaling analysis with second layer density as the tuning parameter,  $\delta = n_c - n$  we find  $\Delta \propto \delta$  consistent with the predicted critical exponents  $z\nu = 1$  for the Bose-Hubbard model in the clean limit in  $d = 2$  dimensions.

## References

- [33] Grafoil Grade GTB, Graftech Inc., Cleveland, USA.
- [34] R. E. Rapp and H. Godfrin, *Phys. Rev. B* **47**, 12004 (1993)
- [35] M. C. Gordillo and D. M. Ceperley, *Phys. Rev. B* **58**, 6447 (1998)
- [36] B. Krishnamachari and G. V. Chester, *Phys. Rev. B* **61**, 9677 (2000)
- [37] M. E. Pierce and E. Manousakis, *Phys. Rev. B* **59**, 3802 (1999)
- [38] P. Corboz, M. Boninsegni, L. Pollet, M. Troyer, *Phys. Rev. B* **78**, 245414 (2008)
- [39] S. van Sciver and O. E. Vilches, *Phys. Rev. B* **18**, 285 (1978)
- [40] D. S. Greywall, *Phys. Rev. B* **41**, 1842 (1990)
- [41] Yongkyung Kwon, D. M. Ceperley, *Phys. Rev. B* **85**, 224501 (2012)
- [42] Jeonghwan Ahn, Hoonkyung Lee, Yongkyung Kwon, *Phys. Rev. B* **93**, 064511 (2016)
- [43] H.J. Lauter, H. Godfrin, V.L.P. Frank, P. Leiderer in *Phase Transitions in Surface Films 2*, ed. H. Taub et al. (Plenum NY), p135.
- [44] H.P. Schildberg, thesis, University of Kiel (1988)
- [45] M. Roger, C. Bäuerle, H. Godfrin, L. Pricoupenko, J. Treiner, *J. Low Temp. Phys.* **112**, 451 (1998)
- [46] P. A. Crowell and J. D. Reppy, *Phys. Rev.* **53**, 2701 (1996)

- [47] J. Nyeki, R. Ray, B. Cowan and J. Saunders, *Phys. Rev. Lett.* **81**, 152 (1998)
- [48] M. Neumann, J. Nyeki, B. Cowan, J. Saunders, *Science* **317**, 1356 (2007)
- [49] F. Ziouzia. Ph. D. thesis (2004), Royal Holloway University of London, unpublished
- [50] On our scale, based on  $^4\text{He}$  second layer promotion at  $11.4 \text{ nm}^{-2}$ , identified by point-B of a vapour pressure isotherm at 4.2K, we find third layer promotion at  $20.0 \text{ nm}^{-2}$ , [48, 49]. Crowell and Reppy [46] take third layer promotion to be  $20.4 \text{ nm}^{-2}$ ; we rescale their coverages by a factor 0.980. Greywall [40] takes third layer promotion to be  $21.2 \text{ nm}^{-2}$ ; we rescale his coverages by a factor 0.943. The heat capacity measurements of the Fukuyama group [54], who use ZYX exfoliated graphite, state good agreement with Greywall, using Grafoil; we rescale their coverages of [54] by the factor 0.943. We also note that the simulations of [37] quote the same third layer promotion as [40], so coverages are scaled by the same factor. The simulations of [38] states promotion to second layer to be  $11.4 \text{ nm}^{-2}$ ; no scaling is applied.
- [51] The non-physical negative values of the dissipation at the lowest temperatures are an artefact of the background subtraction: we are using the empty cell background, so the result indicates that the visco-elastic response of graphite + film leads to lower dissipation at the lowest temperatures. This effect has also been seen in measurements on non-superfluid sub-monolayer helium films on graphite.
- [52] G. Agnolet, D. F. McQueeney and J. D. Reppy, *Phys. Rev. B* **39**, 1934 (1989)
- [53] D. S. Greywall, *Phys. Rev. B* **47**, 309 (1993)
- [54] S. Nakamura, K. Matsui, T. Matsui and H. Fukuyama, *Phys. Rev. B* **94**, 180501(R) (2016)
- [55] A. F. Andreev and I. F. Lifshitz, *Sov. Phys. JETP* **29**, 1107 (1969)
- [56] Y Shibayama, H. Fukuyama and K. Shirahama, *J. Phys:Conference Series* **150**, 032096 (2009)
- [57] R. P. Feynman, “Statistical Mechanics”, Addison-Wesley (1972)
- [58] We note that our experimental determination of the various length scales in exfoliated graphite samples, as part of a programme of substrate development, point to quite different characteristic sizes, depending on the measurement. We intercompare Grafoil, ZYX, and a newer substrate we produced by controlled exfoliation of single crystals. Different relative characteristic sizes emerge from x-ray diffraction, AFM and electronic transport. The smallest of these is 60 nm (Grafoil) from an analysis of x-ray diffraction, which must be considered a lower bound. But significant improvements in the characteristic size inferred from AFM and electron transport in the higher quality material are accompanied by < factor 1.5 increase in crystallite size.
- [59] P.M. Chaikin and T.C. Lubensky, “Principles of Condensed Matter Physics”, CUP (1995)